

# XAI Benchmark for Visual Explanation

Yifei Zhang, Siyi Gu, James Song, Bo Pan, Guangji Bai, Liang Zhao  
Emory University  
Atlanta, GA, United States

{yifei.zhang2, carrie.gu, james.song2, bo.pan, guangji.bai, liang.zhao}@emory.edu

## Abstract

*The rise of deep learning has ushered in significant progress in computer vision (CV) tasks, yet the “black box” nature of these models often precludes interpretability. This challenge has spurred the development of Explainable Artificial Intelligence (XAI) by generating explanations to AI’s decision-making process. An explanation is aimed to not only faithfully reflect the true reasoning process (i.e., faithfulness) but also align with humans’ reasoning (i.e., alignment). Within XAI, visual explanations employ visual cues to elucidate the reasoning behind machine learning models, particularly in image processing, by highlighting images’ critical areas important to predictions. Despite the considerable body of research in visual explanations, standardized benchmarks for evaluating them are seriously underdeveloped. In particular, to evaluate alignment, existing works usually merely illustrate a few images’ visual explanations, or hire some referees to report the explanation quality under ad-hoc questionnaires. However, this cannot achieve a standardized, quantitative, and comprehensive evaluation. To address this issue, we develop a benchmark for visual explanation, consisting of eight datasets with human explanation annotations from various domains, accommodating both post-hoc and intrinsic visual explanation methods. Additionally, we devise a visual explanation pipeline that includes data loading, explanation generation, and method evaluation. Our proposed benchmarks facilitate a fair evaluation and comparison of visual explanation methods. Building on our curated collection of datasets, we benchmarked eight existing visual explanation methods and conducted a thorough comparison across four selected datasets using six alignment-based and causality-based metrics. Our benchmark will be accessible through our website: <https://xaidataset.github.io>.*

## 1. Introduction

Deep Neural Networks (DNNs) have demonstrated remarkable performance in various computer vision (CV) tasks, leading to their widespread application. However, the “black

box” nature of DNNs poses challenges in ensuring the interpretability and reasonableness of AI decisions [1, 43]. In response, Explainable AI (XAI) that aimed at understanding the underlying rationales behind model decision-making in the CV domain [8, 35] has gained significant attention, especially for tasks like image classification. XAI provides visual explanations that empower users to better understand and trust AI-driven decisions for image classifications, thus promoting enhanced transparency and accountability, and facilitating the detection of potential biases or limitations. Visual explanation methods typically aim to identify the most salient regions within an image that are crucial for a model’s prediction, ensuring that these regions not only faithfully reflect the model’s focus but also align with human reasoning. These areas are commonly visualized through saliency maps, which may also be termed heatmaps or attention maps [22, 46, 51]. To be more specific, there are three main categories of visual explanation methods namely: gradient-based methods [38, 41, 42, 49], perturbation-based methods [29, 31, 34], and attention-based methods [14, 16, 28]. Although the aforementioned visual explanation methods are predominantly post-hoc methods, those attention-based methods can be intrinsic when integrated into the model’s architecture as the attention weights highlight the regions of the input that the model deems significant during the prediction process [45].

Current existing works on visual explanation [29, 34, 38, 42, 49] primarily focused on evaluating the *faithfulness* of the explanation, which refers to the degree to which the generated explanation accurately represents the reasoning process of the model, using evaluation methods such as Insertion and Deletion [34]. However, evaluating the *alignment* between model-generated explanations and human rationale remains challenging. Current works mainly employ user interfaces [18, 38] or questionnaires for assessment [13, 34, 38], which are not scalable for large experiments because of the high cost of human assessment and tend to introduce high variance due to their subjective nature and dependency on the evaluator’s perspective. This absence of human explanation annotations and standardized benchmarks not only hinders

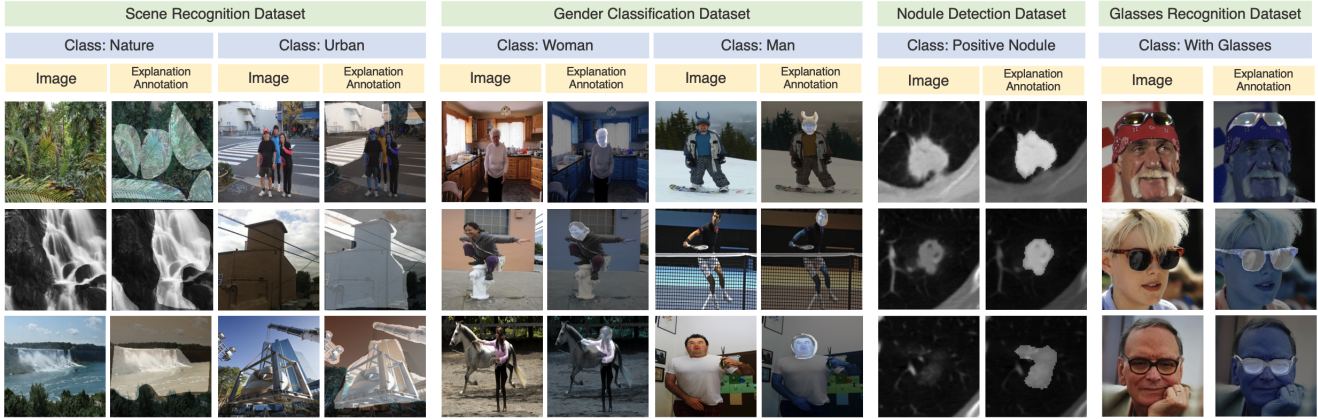


Figure 1. Examples of images and human explanation annotations from our published dataset collection for four selected datasets.

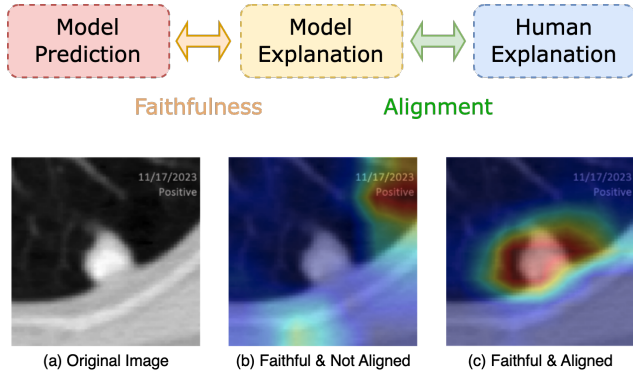


Figure 2. Illustration of *faithfulness* and *alignment*: (a) Original Image; (b) Explanation faithful to model prediction but not aligned with human explanation; (c) Explanation faithful to the model prediction and aligned with human explanation.

the development and equitable assessment of visual explanation methods but also poses significant challenges to the reproducibility and validation of results. Moreover, the lack of universally recognized benchmarks prevents consistent and meaningful cross-study comparisons. An example is shown in Figure 2. When training a DNN model for nodule image classification using a dataset where all “positive” samples (images with nodules) bear a watermark and “negative” samples (images without nodules) do not, there is a risk that the model may learn to classify based on the presence of the watermark rather than the nodule itself. Consequently, the visual explanation for its predictions might appear faithful (as illustrated in Figure 2 (b)) but may not correspond with the understanding of a human expert or domain rationale. Ideally, we aim for visual explanations that are not only faithful to the model’s predictions but also aligned with expert rationale, as demonstrated in Figure 2 (c), where the model has learned to identify the nodule area correctly.

To address the challenges aforementioned, we introduce

our XAI Benchmark for Visual Explanation. An overview is shown in Figure 3. The principal contributions of our work are summarized as follows:

- We publish a dataset collection. Our published collection encompasses eight datasets covering a diverse array of topics including gender classification, object classification, scene classification, nodule classification, tumor detection, and prohibited item detection. Each image within these datasets is annotated with a class label and a human explanation (Figure 1).
- We provide open-source implementations and ready-to-use Application programming interface (API) for the data loading of eight published datasets, eight state-of-the-art visual explanation methods, as well as four alignment-based and two causality-based metrics to evaluate the performance of visual explanation methods.
- We benchmark and analyze the commonly used visual explanation methods using our proposed framework on our published datasets, identifying several limitations and opportunities for improvement.

## 2. Related Work

In XAI domain, there are established benchmark datasets for text and tabular data, largely due to the more accessible nature of their rationales. Similarly, benchmarks for graph data also exist. However, the development of benchmark datasets for image data remains limited, as images present a more complex challenge for providing human explanation annotations. This section introduces the existing works on XAI datasets across text, tabular, graph, and image data.

**XAI Datasets for Text Data.** ERASER [12] is a Natural Language Processing (NLP) benchmark consisting of repurposed and augmented corpora with human-annotated rationales for decisions [12]. Also, textual rationales can be easily gathered from platforms like forums [7, 23, 48] for evaluation. In the NLP domain, there are several works re-

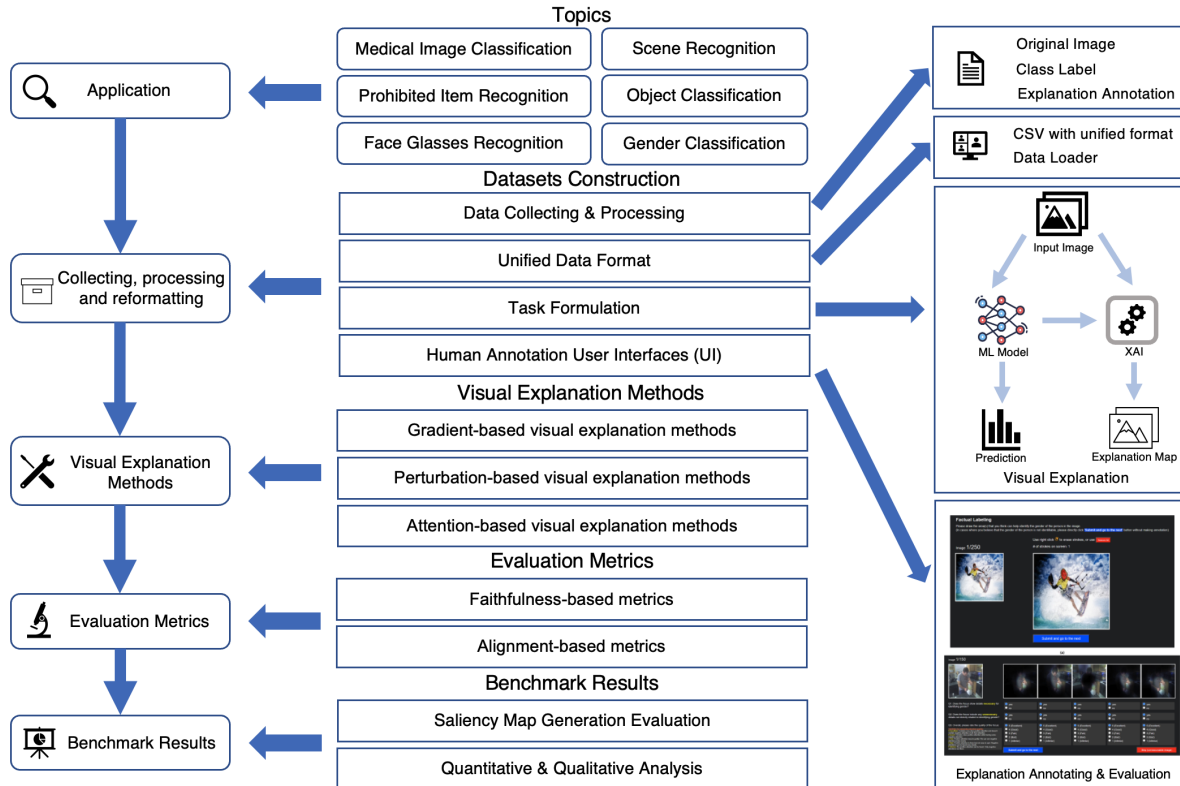


Figure 3. Overview of proposed XAI Benchmark for Visual Explanation.

garding evaluating model-generated rationale against human-annotated rationale using metrics such as ROUGE, BLEU, as well as sufficiency-accuracy [7, 9, 19].

**XAI Datasets for Tabular Data.** XAI-Bench [27] is a collection of synthetic datasets for tabular data with known ground truth distributions that enables the computations of evaluation metrics and thus the evaluations of feature attribution methods [27]. Moreover, besides featuring a synthetic data generator, OpenXAI [3] also provides more evaluation metrics and seven real-world datasets [3].

**XAI Datasets for Graph Data.** SHAPEGGEN [4] is a synthetic dataset generator with ground truth explanations for benchmarking graph neural network (GNN) explainers [4]. Hruska, Zhao, and Liu [21] proposed a ground truth explanation dataset for chemical property prediction on molecular graphs. G-XAI Bench [2] provides a framework with collections of synthetic and real-world graph datasets to compare and evaluate the reliability of GNN explanations.

**XAI Datasets for Image Data.** CLEVR-XAI [6] is a benchmark focused on evaluating visual explanations of visual Question Answering (VQA) tasks with questions and ground truth masks. ImageNet Large Scale Visual Recognition Challenge (ILSVRC) [37] is a benchmark for object detection and classification with millions of images [49]. The Pascal VOC 2012 is another dataset for object recognition [10].

Other datasets include MNIST, CIFAR-10, CIFAR-100, etc., which are also popular for image classification. However, those datasets often lack the use of ground-truth-centered evaluations due to the absence of benchmarks with ground-truth annotations [44]. Sourcing rationales for image data is challenging. Existing evaluations of visual explanation methods still rely on surveys or questionnaires [13, 34, 38] from human judgment without task-specific criteria. Gao et al. and Selvaraju et al. [18, 38] introduced User Interfaces (UIs) to evaluate model-generated visual explanations based on human readability.

### 3. Proposed Datasets and Benchmark

In this section, we introduce our proposed XAI Benchmark for Visual Explanations. We begin by presenting a newly constructed dataset collection, providing both an overview of the dataset collection and a detailed introduction to each dataset. Subsequently, we present the formulation and evaluation metrics for visual explanation tasks.

#### 3.1. Dataset Collection

To construct our dataset collection for visual explanation, we first collected images from eight publicly available and widely-used datasets covering a range of topics, including

gender classification, object classification, scene recognition, nodule classification, tumor classification, and prohibited item recognition. For the gender classification task, salient regions typically encompass facial features, which are critical for accurate classification. In the context of nodule classification, saliency may extend to both intranodular and perinodular areas, varying with the nodule’s characteristics. Conversely, for object classification, salient areas are consistently localized to the object in question. Scene recognition presents a more complex scenario, where saliency is distributed across multiple regions contributing to the scene’s categorization. Illustrative examples of these saliency distributions are depicted in Figure 1. To annotate these datasets, we employed methodologies including human annotation and foreground extraction, thereby providing robust ground-truth explanations for model evaluation. To facilitate the human annotating, we developed a user interfaces (UIs) designed to capture regions of interest that humans intuitively associate with the classification decisions. These interfaces facilitate the collection of saliency annotations that reflect the cognitive underpinnings of human visual judgment, aligning with principles from the XAI domain [47]. In Table 1, we summarized the general profiles for eight published datasets.

**Gender Classification Dataset (Gender-XAI)** The gender classification dataset is derived from the Microsoft COCO dataset [26]. To construct the dataset, we extracted images from the COCO dataset that contained captions with the terms *man* or *woman*. Further filtering was performed to remove images that mentioned both genders in the caption, depicted multiple individuals, or featured unrecognizable human figures. Furthermore, a subset of the images was manually annotated by human annotators using human annotation user interfaces (UIs), resulting in *factual* and *counterfactual* masks. This process yielded *factual* masks for images where the captioned gender is clearly present (*positive* labels), and *counterfactual* masks for those where the captioned gender is not visually identifiable (*negative* labels). The UIs are designed for both annotation and evaluation purposes [17, 18]. The dataset comprises a total of 1,736 images, each with a class label and human explanation annotation, evenly distributed between females and males.

**Scene Recognition Dataset (Scene-XAI)** The scene recognition dataset used in our study is derived from the Places365 dataset [50]. The dataset was further annotated manually by Gao et al. [17, 18] with human annotation user interfaces (UIs) to obtain *factual* and *counterfactual* masks, examples are shown in 4. The task of this dataset involves binary classification for scene recognition, specifically distinguishing between natural and urban scenes. To create the dataset, we selectively sampled images from specific categories. Specifically, the categories used to sample the data are: *Nature*: mountain, pond, waterfall, field wild, forest broadleaf, rainforest; and *Urban*: house, bridge, campus, tower, street,

driveway. In total, the dataset comprises 2,086 images, each with a class label and human explanation annotation.

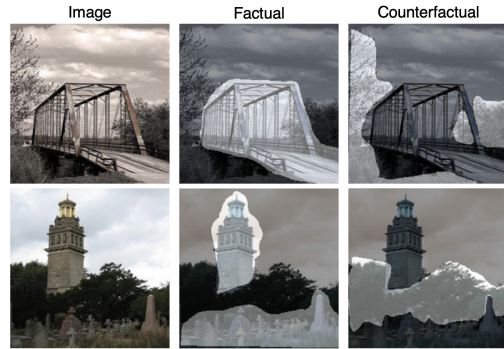


Figure 4. Examples of factual and counterfactual masks.

**Face Glasses Recognition Dataset (Glasses-XAI)** The face glasses recognition dataset is derived from the CelebAMask-HQ dataset [25]. This dataset is initially categorized to distinguish face images with and without glasses. CelebAMask-HQ includes manually annotated masks of 19 classes encompassing various facial features and accessories. We utilized the segmentation masks of eyes and glasses to derive factual labels for glasses recognition. The dataset comprises 885 images, each with a class label and corresponding human explanation annotations.

**Prohibited Item Recognition Dataset (Prohibited-XAI)** The prohibited item recognition task in our study is constructed using the Sixray dataset [30]. The Sixray dataset, partitioned based on the recognition of prohibited items, comprises an extensive suite of 1,059,231 X-ray images. Each image is annotated at the image level by experienced security inspectors, whose expert annotations we repurpose as human explanation annotations. This approach capitalizes on professional insight, ensuring that our dataset’s annotations reflect real-world classification scenarios and provide a reliable basis for the binary classification of prohibited items. Consequently, each image is labeled with both a class label and a corresponding ground-truth explanation annotation.

**Nodule Classification Dataset (Nodule-XAI)** We constructed the nodule classification dataset from the LIDC-IDRI [5], which comprises thoracic computed tomography (CT) scans from lung cancer screenings annotated with lesion markers. We converted the 3D nodule images into 2D by selecting the central slice along the z-axis and resizing it to 224×224 pixels. Up to four experienced thoracic radiologists provided annotations in XML format for each scan. The ground truth explanation was established by computing a consensus volume from these annotations, with a nodule considered *positive* if agreed upon by at least 50% of the radiologists. Conversely, *negative* samples were derived by slicing surrounding areas without nodules. Post-preprocessing, the dataset includes 2,625 *positive* nodule images and 65,505 *negative* non-nodule images. The primary objective of uti-

Dataset	Class Type	Size	Annotation Type	Format	Balanced	Counterfactual
Gender-XAI	Binary	1,736	Human annotation	Pixel-wise	✓	✓
Scene-XAI	Binary	2,086	Human annotation	Pixel-wise	✓	✓
Glasses-XAI	Binary	885	Human annotation	Pixel-wise	✓	✗
Prohibited-XAI	Binary	1,059,231	Human annotation	Bounding-box	✗	✗
Nodule-XAI	Binary	2,625	Human annotation	Pixel-wise	✗	✗
Tumor-XAI	Binary	281	Human annotation	Pixel-wise	✗	✗
Cat&Dog-XAI	Multi-class	7,349	Foreground extraction	Pixel-wise	✓	✗
Object-XAI	Multi-class	11,540	Foreground extraction	Pixel-wise	✓	✗

Table 1. Summary of Currently Available Datasets: The column labeled “Class Type” indicates the number of classes included in each dataset. “Size” describes the total count of images, class labels, and explanation annotation pairs within the dataset. “Annotation Type” delineates the source of the explanation annotations. “Format” specifies the manner in which the explanation annotations are presented. The “Balanced” column signifies whether the dataset maintains balance in terms of the predictive label, while the “Counterfactual” column indicates the provision of counterfactual explanation annotations.

lizing this dataset is to determine the presence or absence of nodules in the images.

**Tumor Classification Dataset (Tumor-XAI)** To construct our dataset, we sourced normal pancreas images from the Cancer Imaging Archive [36]. Abnormal scans, featuring pancreatic tumors, were derived from the Medical Segmentation Decathlon dataset (MSD), where initial ground-truth annotations by a medical student were rigorously reviewed and refined by a skilled radiologist. The final dataset includes 281 *positive* scans, identified by the presence of tumors, and 80 *negative* scans without tumor indications. In a preprocessing approach akin to that used for the LIDC-IDRI dataset, we converted the 3D scans into 2D slices by randomly selecting along the z-axis, thus setting the stage for a binary classification task to discern between *positive* (tumorous) and *negative* (normal) pancreatic samples.

**Cats and Dogs Classification Dataset (Cat&Dog-XAI)** The Cats and Dogs Classification Dataset used in our study is constructed from The Oxford-IIIT Pet Dataset [33]. This dataset, tailored for pet image analysis, contains over 7,000 images across 37 unique categories, each corresponding to different breeds of dogs or cats. For the purposes of our research, we treat pixel-level foreground extractions, which isolate the pet from the background, as proxies for human explanation annotations. These extractions effectively highlight the subject of interest in alignment with the class label, mirroring the focus areas a human annotator might identify when asked to explain the basis for classifying an image as either a *dog* or a *cat*.

**Object Classification Dataset (Object-XAI)** The Object Classification Dataset utilized in our study is constructed from the PASCAL VOC 2012 Dataset [15]. The dataset comprises roughly 11,540 images images and covers 20 diverse object categories. These include *cars*, *dogs*, *chairs*,

*people*, *bicycles*, *cats*, *horses*, *birds*, *boats*, *aeroplanes*, *buses*, *trains*, *motorcycles*, *cows*, *dining tables*, *potted plants*, *sheep*, *sofas*, *TVs*, and *bottles*. Each image in the VOC 2012 Dataset is manually annotated with pixel-level region masks and corresponding class labels for identified objects, providing a robust resource for object classification research. In our study, explanation annotations were generated by extracting the pixel-level foreground corresponding to the image label class, leveraging these precise regions as effective proxies for human explanations by directly highlighting the areas most relevant to the object’s classification.

### 3.2. Visual Explanation Formulation

The primary goal of visual explanation methods in XAI is to render the decision-making process of AI models handling visual data intelligible and transparent, by highlighting which features of the input influence the predictions. Formally, in the image classification domain, the visual explanation problem can be defined as follows: Given a predictive model  $f$  that maps an input image  $I$  to an output  $y$  (e.g., class labels), the goal of a visual explanation method is to generate a visual explanation  $E$  (e.g., heatmaps, saliency maps, and attention maps) which visually represents the contribution of different parts of  $I$  towards the prediction  $y$ . Formally, the predictive model describes  $f : I \rightarrow y$  and the explanation function  $g$  takes the predictive model  $f$  and the input  $I$  and produces the explanation  $E$ , which can be described as  $E = g(f, I)$ , where  $g$  can be either intrinsic or post-hoc visual explanation methods. The faithfulness of explanation can be expressed as  $h(E, f, I)$  which evaluates how the model-generated explanation  $E$  influences the corresponding model’s prediction. The alignment of explanation is expressed as  $d(E, A)$ , where  $d$  is a function that measures the difference between model-generated explana-

tion  $E$  and ground-truth explanation annotations  $A$  (such as IoU, precision, recall, and  $\mathcal{L}-1$  loss).

### 3.3. Evaluation Metric

Our benchmark provides accessible implementations for a wide range of quantitative metrics established by previous studies. We divide these metrics into two categories: 1) Alignment-based metrics, which assess how well explanations match human-annotated ground truth, and 2) Faithfulness-based metrics, which evaluate how well explanations reflect the actual workings of the model. Below, we offer detailed explanations of both types of metrics.

#### 3.3.1 Alignment-based metrics

Alignment-based metrics measure how well the explanations generated by a method align with human explanation annotation as  $d(E, A)$ . These metrics include IoU, precision, recall, F1-score, and Pointing Game. To compute IoU, precision, and recall,  $E$  must be first converted into a binary map that can be directly compared with the binary human explanation annotations  $A$ . Each pixel of the binary explanation map  $B$  can be represented as follows:

$$B(x, y) = \begin{cases} 1 & \text{if } E(x, y) \geq \theta \\ 0 & \text{otherwise} \end{cases}$$

, where  $(x, y)$  represents the pixel coordinates in  $E$  and  $\theta$  denotes the chosen threshold.

**Intersection over Union (IoU)** IoU is a common metric that measures the overlap between two sets. For visual explanations, it compares the overlap between the salient regions identified by the model and those annotated by humans.

$$\text{IoU} = \frac{|B \cap A|}{|B \cup A|}$$

**Precision** evaluates the exactness of  $B$ , the proportion of identified salient regions in  $B$  that are also in  $A$ .

$$\text{Precision} = \frac{|B \cap A|}{|B|}$$

**Recall** measures the completeness of  $B$ , the proportion of actual salient regions in  $A$  that are correctly identified in  $B$ .

$$\text{Recall} = \frac{|B \cap A|}{|A|}$$

**F1 Score** The F1 score is the harmonic mean of precision and recall, providing a balance between the two by penalizing extreme values.

$$\text{F1} = 2 \times \frac{\text{Precision} \times \text{Recall}}{\text{Precision} + \text{Recall}}$$

**Pointing Game** The Pointing Game [34] evaluates if the peak of the explanation  $E$  falls within the human explanation annotation  $A$ :

$$\text{Pointing Game} = \frac{\sum_{i=1}^N 1[\text{MaxLoc}(E_i) \in A_i]}{N}$$

where  $N$  is the number of samples, and  $\text{MaxLoc}(E_i)$  is the location of the highest activation in the explanation map  $E$  for the  $i$ -th sample.

#### 3.3.2 Faithfulness-based metrics

Faithfulness-based metrics assess the causal effect that highlighted features in an explanation have on the model’s output as  $h(E, f, I)$ . In other words, they test whether manipulating the parts of the input deemed important by the explanation actually changes the model’s prediction in a predicted manner. These faithfulness-based metrics, including the Average Drop % score, Deletion, Insertion, and Adversarial perturbation, provide a robust framework for evaluating the extent to which a model’s explanations reflect actual causal relationships rather than mere correlations in the model’s reasoning process.

**The Average Drop % score:** The Average Drop % score assesses the significance of regions highlighted by visual explanation methods. It quantifies the decrease in a model’s performance when the identified regions are masked. A significant drop indicates that the highlighted regions of the image are vital for the model’s decisions. This metric helps validate the effectiveness of visual explanations, ensuring that the pinpointed areas in images genuinely influence the model’s predictions [10].

**Deletion:** Deletion is a way of testing how much the prediction score changes when you remove the most important features, as identified by the explanation. In the context of image classification, for example, you’d remove (or occlude) the most important parts of the image and see how much the model’s confidence in its prediction decreases. Formally, the Deletion metric  $D$  can be calculated as  $D = \int_0^1 P(y|I_{\text{remove}}(r))dr$ , where  $P(y|I_{\text{remove}}(r))$  is the probability of the predicted class  $y$  given the input image  $I$  with a fraction  $r$  of the most important pixels removed.

**Insertion:** Insertion tests how much the prediction score changes when you add the most important features, starting from a blank image. You gradually insert the most important parts of the image, as identified by the explanation, and see how much the model’s confidence in its prediction increases. If the explanation is good, then inserting the parts of the image it highlights should increase the prediction confidence significantly. Formally, The Insertion metric  $I$  can be calculated as  $I = \int_0^1 P(y|I_{\text{insert}}(r))dr$ , where  $P(y|I_{\text{insert}}(r))$  is the probability of the predicted class  $y$  given the input image  $I$  with a fraction  $r$  of the most important pixels kept.

## 4. Benchmark Experiments

In this section, we detail our benchmarking of state-of-the-art visual explanation methods using our published datasets. We begin by outlining the experimental setup, followed by the presentation of benchmarking results and analysis.

### 4.1. Experimental Setup

**Visual Explanation Methods.** We choose eight common visual explanation methods. For Gradient-based Methods, we choose CAM [49], GradCAM [38], GradCAM++ [10], IntegratedGradients (IG) [42], GuidedBackpropagation (GBP) [32], Saliency [40], and InputXGradient (IxG) [39]. For the Perturbation-based method, we choose RISE [34]. For Attention-based method, we choose ViT [14]. We utilize the ResNet-18 architecture [20] pre-trained on ImageNet [11] and ViT with vit-base-patch16-224 architecture as backbone image classifiers, fine-tuning only the final fully connected layer to match the class count of our target dataset. We adhere to the default hyperparameter settings for the visual explanation models as specified in their original implementations. The models undergo 30 epochs of training using the Adam optimizer [24] with a learning rate of 0.0001. Our experiments are implemented based on PyTorch and performed on an NVIDIA GTX 3090 GPU.

**Evaluation Metrics.** The assessment of the performance of visual explanation methods is conducted using four widely recognized alignment-based evaluation metrics: Intersection over Union (IoU), Precision, Recall, and the Pointing Game. These metrics facilitate comparison of the generated explanations with our proposed human explanation ground truth. Moreover, we utilize two faithfulness-based evaluation metrics, Insertion and Deletion. Our benchmark evaluation spans across the Gender-XAI, Scene-XAI, Cat&Dog-XAI, and Object-XAI datasets.

**Data Preparation.** For each experiment, we allocated the samples as follows: 60% for training, 20% for validation, and the remaining 20% for testing. Specifically, for the Object dataset, which includes multiple classes, our experiment focused on three specific classes—bird, horse, and sheep—totaling 765 samples.

### 4.2. Result and Analysis

In this section, we present the results and analysis of our benchmarking experiments. Initially, we offer a quantitative analysis of the experimental outcomes for various visual explanation methods across different datasets. This is followed by a qualitative analysis of the visualization results from the previous experiments. Additionally, we conduct an Inter-method Reliability Analysis to examine the correlations between different visual explanation methods based on our benchmarking experiments.

**Quantitative Analysis** From Table 3, we can observe that we can observe that RISE outperforms other methods in

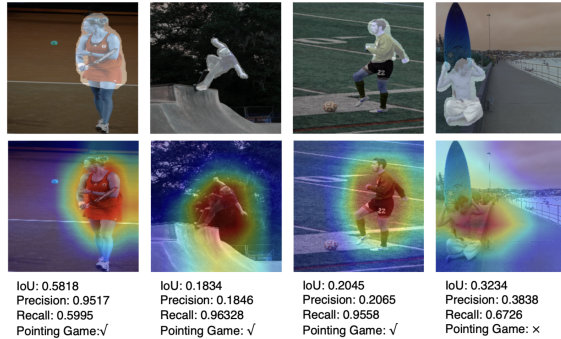


Figure 5. Examples of alignment-based evaluations (IoU, Precision, Recall, and Pointing Game) comparing saliency maps generated by Grad-CAM with human explanation annotations.

most of the datasets. Notably, RISE takes advantage of its model-agnostic nature, its ability to provide a global interpretation of the model’s decisions, its inherent robustness, and its potential to better handle multi-modal inputs. Its strategy of aggregating predictions over multiple randomly sampled binary masks could lead to more stable and reliable explanations. ViT achieves best alignment performance in gender classification. It tends to excel in visual explanation tasks on large-scale datasets but underperforms on smaller ones, likely due to its substantial computational demands and the need for more extensive training data inherent to transformer-based models. Methods like CAM, GradCAM, and GradCAM++ excel in the Pointing Game due to their ability to leverage network layers for high-resolution feature capture, aiding precise localization. Conversely, while the Pointing Game emphasizes accuracy, IoU, Precision, and Recall measure overall object coverage, which may explain the varied performance across these metrics. For perturbation-based metrics like insertion and deletion, which forego ground truth annotations, RISE outperforms other methods, reaffirming its effectiveness even against ground truth-reliant aligned-based evaluation methods.

We also performed an inter-method reliability analysis [44] to determine the consistency between different metrics in evaluating explanation quality. Spearman rank and point-biserial correlations were utilized to measure associations between continuous and binary-to-continuous outcomes, respectively. Standardized ranks were applied where necessary. The analysis covered four visual explanation methods—GradCAM, IG, RISE, and ViT—using two alignment-based metrics (IoU and Pointing) and two faithfulness-based metrics (insertion and deletion). The correlation results, presented in Table 2, reveal a negative correlation between insertion and deletion for IG, suggesting divergent quality assessments. This pattern is not mirrored by the other methods. Across all methods, deletion and Pointing Game metrics consistently show negative correlation. GradCAM and RISE exhibit comparable correlation

trends, in contrast to IG’s unique pattern, potentially due to its sparse explanations.

Correlation coefficients	GradCAM	IG	RISE	ViT
Insertion & Deletion	+0.5	-0.3	+0.1	+0.3
Insertion & Pointing	+0.6	+0.1	+0.3	+0.4
Insertion & IoU	+0.7	+0.3	+0.3	+0.4
Deletion & Pointing	-0.9	-0.6	-0.9	-0.8
Deletion & IoU	-0.8	-0.2	-0.6	-0.8
Pointing & IoU	+0.9	-0.1	+0.7	+1.0

Table 2. The pairwise Spearman correlation coefficient between different evaluation metrics for inter-method reliability analysis

**Qualitative Analysis** Figure 6 illustrates various visual explanation maps generated by leading explanation methods, including GradCAM, ViT, and InputXGradient, to provide a qualitative assessment of their interpretative capabilities. The explanation maps by InputXGradient are typically characterized by sparsely distributed focal points, offering a stark contrast to the broader, more contiguous heatmaps produced by other methods, which tend to align closely with human perceptual patterns. Despite these structural differences, each method effectively identifies and emphasizes the pivotal regions influencing the image classification decision. Saliency maps derived from GradCAM are notable for their targeted focus on singular, significant regions, with the gran-

ularity of the map boundaries influenced by the underlying CNN architecture employed. This can result in smoother transitions at the edges of highlighted areas, facilitating a clearer demarcation of relevant features. In the case of ViT, the explanation maps produced are rich in detail, reflecting the model’s ability to process complex interrelations across the image due to the global receptive field afforded by the self-attention mechanism. The ViT maps often capture multiple relevant regions, providing a comprehensive visualization of the factors contributing to the model’s prediction. This multi-faceted approach allows for an enhanced understanding of the model’s reasoning, particularly in scenarios where the decision-making process is distributed across the image rather than localized to a single feature. These visual explanation techniques, each with their unique way of interpreting model decisions, offer valuable insights into the model’s focus areas.

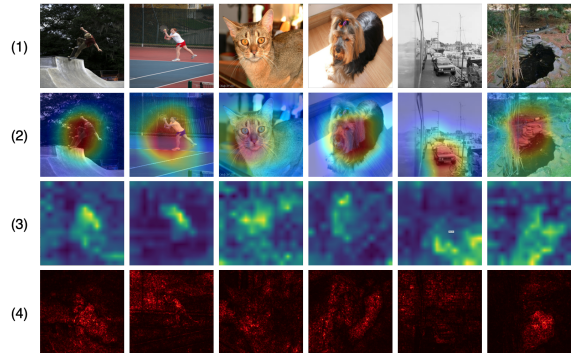


Figure 6. Qualitative results of visual explanation methods: (1) Original image; (2) Saliency map generated by Grad-CAM; (3) Attention map generated by Vision Transformer (ViT); (4) Gradient-based saliency map generated by InputXGradient.

Dataset	Model	Alignment				faithfulness	
		IoU	Precision	Recall	Pointing	Insertion	Deletion
Gender-XAI	CAM	0.1429	0.5396	0.5577	0.3077	0.688	0.123
	GradCAM	0.1304	0.5371	0.5677	0.2901	0.696	0.129
	GradCAM++	0.1417	0.5379	0.5644	0.2906	0.663	0.152
	IG	0.3441	0.7939	0.7232	0.2138	0.363	0.252
	GBP	0.3542	0.8076	0.7343	0.2931	0.397	0.228
	IxG	0.3403	0.6345	0.6712	0.3011	0.401	0.248
	Saliency	0.3229	0.7831	0.6620	0.3208	0.381	0.233
	RISE	0.3416	0.7875	0.7285	0.3307	0.845	0.101
	ViT	0.3698	0.7827	0.6984	0.3802	0.671	0.134
	Scene-XAI	CAM	0.3704	0.7625	0.4988	0.3852	0.711
GradCAM		0.3656	0.7637	0.5096	0.4777	0.691	0.110
GradCAM++		0.3632	0.7637	0.4977	0.4224	0.701	0.104
IG		0.5356	0.8144	0.6368	0.2810	0.511	0.201
GBP		0.4832	0.8456	0.5842	0.3277	0.582	0.211
IxG		0.4566	0.8272	0.7043	0.3010	0.572	0.226
Saliency		0.5104	0.8523	0.6612	0.3100	0.491	0.206
RISE		0.5428	0.8675	0.6674	0.3624	0.923	0.109
ViT		0.5263	0.8425	0.6842	0.3857	0.763	0.115
Cat&Dog-XAI		CAM	0.1284	0.1285	0.8437	0.3121	0.736
	GradCAM	0.1599	0.1641	0.8116	0.3121	0.752	0.343
	GradCAM++	0.1236	0.1239	0.8349	0.3434	0.766	0.351
	IG	0.3002	0.3003	0.9974	0.1728	0.399	0.270
	GBP	0.3026	0.3029	0.9973	0.2184	0.472	0.301
	IxG	0.2808	0.3062	0.9244	0.1892	0.468	0.317
	Saliency	0.2978	0.3049	0.9741	0.2136	0.422	0.290
	RISE	0.3094	0.3095	0.9987	0.1628	0.886	0.236
	ViT	0.2895	0.2931	0.9457	0.2514	0.792	0.291
	Object-XAI	CAM	0.0524	0.0527	0.3731	0.1667	0.613
GradCAM		0.0518	0.0518	0.3808	0.1993	0.667	0.351
GradCAM++		0.0515	0.0516	0.3664	0.1933	0.629	0.378
IG		0.1389	0.3395	0.4998	0.2000	0.397	0.214
GBP		0.1250	0.3252	0.4918	0.1382	0.440	0.283
IxG		0.1312	0.3553	0.4010	0.1640	0.433	0.291
Saliency		0.1445	0.3287	0.4299	0.1301	0.303	0.217
RISE		0.1423	0.3423	0.5266	0.1400	0.857	0.211
ViT		0.1416	0.3388	0.5179	0.1743	0.445	0.264

Table 3. Quantitative evaluation and comparison of visual explanation models on published datasets. The best results for each task are bolded and the second bests are underlined.

## 5. Conclusion and Limitation

Our work releases an XAI benchmark for visual explanation that consists of eight distinct datasets across topics like object classification and medical image classification. Comprehensive benchmarking experiments were carried out on four datasets, applying various visual explanation models and evaluation metrics. This thorough analysis offered valuable insights into model interpretability. We also created an API for data loading and made easy-to-use evaluation metric code available on our website, enhancing ease in assessing visual explanation methods. These efforts aim to foster advancement and further research in XAI.

Our benchmark aims to fill the gap of missing ground truth explanations for evaluating visual explanation methods, yet it is not without potential limitations. In our Gender Classification and Scene Recognition datasets, human annotators provide ground-truth explanations, which, despite rigorous independent assessments, may still introduce indi-



vidual biases. Also, regarding the pancreatic tumor detection dataset, the negative and positive samples are sourced from different sources. This situation introduces a potential bias wherein the classifiers could inadvertently learn to predict the image source—a variable inherently aligned with the label—instead of focusing on the crucial causal information, such as the tumor’s actual location.

## References

- [1] A. Adadi and M. Berrada. Peeking inside the black-box: a survey on explainable artificial intelligence (xai). *IEEE access*, 6:52138–52160, 2018. [1](#)
- [2] C. Agarwal, O. Queen, H. Lakkaraju, and M. Zitnik. An explainable ai library for benchmarking graph explainers. 2018. [3](#)
- [3] C. Agarwal, S. Krishna, E. Saxena, M. Pawelczyk, N. Johnson, I. Puri, M. Zitnik, and H. Lakkaraju. Openxai: Towards a transparent evaluation of model explanations, 2023. [3](#)
- [4] C. Agarwal, O. Queen, H. Lakkaraju, and M. Zitnik. Evaluating explainability for graph neural networks, 2023. [3](#)
- [5] S. G. Armato III, G. McLennan, L. Bidaut, M. F. McNitt-Gray, C. R. Meyer, A. P. Reeves, B. Zhao, D. R. Aberle, C. I. Henschke, E. A. Hoffman, et al. The lung image database consortium (lidc) and image database resource initiative (idri): a completed reference database of lung nodules on ct scans. *Medical physics*, 38:915–931, 2011. [4](#)
- [6] L. Arras, A. Osman, and W. Samek. Clevr-xai: A benchmark dataset for the ground truth evaluation of neural network explanations. *Information Fusion*, 81:14–40, 2022. ISSN 1566-2535. doi: <https://doi.org/10.1016/j.inffus.2021.11.008>. URL <https://www.sciencedirect.com/science/article/pii/S1566253521002335>. [3](#)
- [7] J. Boyd-Graber, S. Carton, S. Feng, Q. V. Liao, T. Lombrozo, A. Smith-Renner, and C. Tan. Human-centered evaluation of explanations. In *Proceedings of the 2022 Conference of the North American Chapter of the Association for Computational Linguistics: Human Language Technologies: Tutorial Abstracts*, pages 26–32, 2022. [2](#), [3](#)
- [8] V. Buhrmester, D. Münch, and M. Arens. Analysis of explainers of black box deep neural networks for computer vision: A survey. *Machine Learning and Knowledge Extraction*, 3: 966–989, 2021. [1](#)
- [9] S. Carton, A. Rathore, and C. Tan. Evaluating and characterizing human rationales. *arXiv preprint arXiv:2010.04736*, 2020. [3](#)
- [10] A. Chattopadhyay, A. Sarkar, P. Howlader, and V. N. Balasubramanian. Grad-cam++: Generalized gradient-based visual explanations for deep convolutional networks. In *2018 IEEE winter conference on applications of computer vision (WACV)*, pages 839–847. IEEE, 2018. [3](#), [6](#), [7](#)
- [11] J. Deng, W. Dong, R. Socher, L.-J. Li, K. Li, and L. Fei-Fei. Imagenet: A large-scale hierarchical image database. In *2009 IEEE conference on computer vision and pattern recognition*, pages 248–255. Ieee, 2009. [7](#)
- [12] J. DeYoung, S. Jain, N. F. Rajani, E. Lehman, C. Xiong, R. Socher, and B. C. Wallace. Eraser: A benchmark to evaluate rationalized nlp models, 2020. [2](#)
- [13] F. Doshi-Velez and B. Kim. Towards a rigorous science of interpretable machine learning. *arXiv preprint arXiv:1702.08608*, 2017. [1](#), [3](#)
- [14] A. Dosovitskiy, L. Beyer, A. Kolesnikov, D. Weissenborn, X. Zhai, T. Unterthiner, M. Dehghani, M. Minderer, G. Heigold, S. Gelly, et al. An image is worth 16x16 words: Transformers for image recognition at scale. *arXiv preprint arXiv:2010.11929*, 2020. [1](#), [7](#)
- [15] M. Everingham, L. Van Gool, C. K. I. Williams, J. Winn, and A. Zisserman. The pascal visual object classes (voc) challenge. *International Journal of Computer Vision*, 88: 303–338, June 2010. [5](#)
- [16] H. Fukui, T. Hiraoka, T. Yamashita, and H. Fujiiyoshi. Attention branch network: Learning of attention mechanism for visual explanation. In *Proceedings of the IEEE/CVF conference on computer vision and pattern recognition*, pages 10705–10714, 2019. [1](#)
- [17] Y. Gao, T. S. Sun, G. Bai, S. Gu, S. R. Hong, and Z. Liang. Res: A robust framework for guiding visual explanation. In *Proceedings of the 28th ACM SIGKDD Conference on Knowledge Discovery and Data Mining*, pages 432–442, 2022. [4](#)
- [18] Y. Gao, T. S. Sun, L. Zhao, and S. R. Hong. Aligning eyes between humans and deep neural network through interactive attention alignment. *Proceedings of the ACM on Human-Computer Interaction*, 6(CSCW2):1–28, 2022. [1](#), [3](#), [4](#)
- [19] C. Garbacea and Q. Mei. Neural language generation: Formulation, methods, and evaluation. *arXiv preprint arXiv:2007.15780*, 2020. [3](#)
- [20] K. He, X. Zhang, S. Ren, and J. Sun. Deep residual learning for image recognition. In *Proceedings of the IEEE conference on computer vision and pattern recognition*, pages 770–778, 2016. [7](#)
- [21] E. Hruska, L. Zhao, and F. Liu. Ground truth explanation dataset for chemical property prediction on molecular graphs. 2022. [3](#)
- [22] M. Ivanovs, R. Kadikis, and K. Ozols. Perturbation-based methods for explaining deep neural networks: A survey. *Pattern Recognition Letters*, 150:228–234, 2021. [1](#)
- [23] D. Khashabi, S. Chaturvedi, M. Roth, S. Upadhyay, and D. Roth. Looking beyond the surface: A challenge set for reading comprehension over multiple sentences. In *Proceedings of the 2018 Conference of the North American Chapter of the Association for Computational Linguistics: Human Language Technologies, Volume 1 (Long Papers)*, pages 252–262, 2018. [2](#)
- [24] D. P. Kingma and J. Ba. Adam: A method for stochastic optimization. *arXiv preprint arXiv:1412.6980*, 2014. [7](#)
- [25] C.-H. Lee, Z. Liu, L. Wu, and P. Luo. Maskgan: Towards diverse and interactive facial image manipulation. In *IEEE Conference on Computer Vision and Pattern Recognition (CVPR)*, 2020. [4](#)
- [26] T. Lin, M. Maire, S. J. Belongie, L. D. Bourdev, R. B. Girshick, J. Hays, P. Perona, D. Ramanan, P. Dollár, and C. L. Zitnick. Microsoft COCO: common objects in context. *CoRR*, abs/1405.0312, 2014. URL <http://arxiv.org/abs/1405.0312>. [4](#)

- [27] Y. Liu, S. Khandagale, C. White, and W. Neiswanger. Synthetic benchmarks for scientific research in explainable machine learning, 2021. [3](#)
- [28] Z. Liu, Y. Lin, Y. Cao, H. Hu, Y. Wei, Z. Zhang, S. Lin, and B. Guo. Swin transformer: Hierarchical vision transformer using shifted windows. In *Proceedings of the IEEE/CVF international conference on computer vision*, pages 10012–10022, 2021. [1](#)
- [29] A. Messalás, Y. Kanellopoulos, and C. Makris. Model-agnostic interpretability with shapley values. In *2019 10th International Conference on Information, Intelligence, Systems and Applications (IISA)*, pages 1–7. IEEE, 2019. [1](#)
- [30] C. Miao, L. Xie, F. Wan, C. Su, H. Liu, J. Jiao, and Q. Ye. Sixray : A large-scale security inspection x-ray benchmark for prohibited item discovery in overlapping images, 2019. [4](#)
- [31] S. Mishra, B. L. Sturm, and S. Dixon. Local interpretable model-agnostic explanations for music content analysis. In *ISMIR*, volume 53, pages 537–543, 2017. [1](#)
- [32] S. Mostafa, D. Mondal, M. A. Beck, C. P. Bidinosti, C. J. Henry, and I. Stavness. Leveraging guided backpropagation to select convolutional neural networks for plant classification. *Frontiers in Artificial Intelligence*, 5:871162, 2022. [7](#)
- [33] O. M. Parkhi, A. Vedaldi, A. Zisserman, and C. V. Jawahar. Cats and dogs. In *IEEE Conference on Computer Vision and Pattern Recognition*, 2012. [5](#)
- [34] V. Petsiuk, A. Das, and K. Saenko. Rise: Randomized input sampling for explanation of black-box models. *arXiv preprint arXiv:1806.07421*, 2018. [1](#), [3](#), [6](#), [7](#)
- [35] T. Rojat, R. Puget, D. Filliat, J. Del Ser, R. Gelin, and N. Díaz-Rodríguez. Explainable artificial intelligence (xai) on time-series data: A survey. *arXiv preprint arXiv:2104.00950*, 2021. [1](#)
- [36] H. R. Roth, L. Lu, A. Farag, H.-C. Shin, J. Liu, E. B. Turkbey, and R. M. Summers. Deeporgan: Multi-level deep convolutional networks for automated pancreas segmentation. In *Medical Image Computing and Computer-Assisted Intervention—MICCAI 2015: 18th International Conference, Munich, Germany, October 5-9, 2015, Proceedings, Part I 18*, pages 556–564. Springer, 2015. [5](#)
- [37] O. Russakovsky, J. Deng, H. Su, J. Krause, S. Satheesh, S. Ma, Z. Huang, A. Karpathy, A. Khosla, M. Bernstein, A. C. Berg, and L. Fei-Fei. Imagenet large scale visual recognition challenge, 2015. [3](#)
- [38] R. R. Selvaraju, M. Cogswell, A. Das, R. Vedantam, D. Parikh, and D. Batra. Grad-cam: Visual explanations from deep networks via gradient-based localization. In *Proceedings of the IEEE international conference on computer vision*, pages 618–626, 2017. [1](#), [3](#), [7](#)
- [39] A. Shrikumar, P. Greenside, A. Shcherbina, and A. Kundaje. Not just a black box: Learning important features through propagating activation differences. *arXiv preprint arXiv:1605.01713*, 2016. [7](#)
- [40] K. Simonyan, A. Vedaldi, and A. Zisserman. Deep inside convolutional networks: Visualising image classification models and saliency maps. *arXiv preprint arXiv:1312.6034*, 2013. [7](#)
- [41] J. T. Springenberg, A. Dosovitskiy, T. Brox, and M. Riedmiller. Striving for simplicity: The all convolutional net. *arXiv preprint arXiv:1412.6806*, 2014. [1](#)
- [42] M. Sundararajan, A. Taly, and Q. Yan. Axiomatic attribution for deep networks. In *International conference on machine learning*, pages 3319–3328. PMLR, 2017. [1](#), [7](#)
- [43] E. Tjoa and C. Guan. A survey on explainable artificial intelligence (xai): Toward medical xai. *IEEE transactions on neural networks and learning systems*, 32:4793–4813, 2020. [1](#)
- [44] B. Vandersmissen and J. Oramas. On the coherence of quantitative evaluation of visual expalantion. *arXiv preprint arXiv:2302.10764*, 2023. [3](#), [7](#)
- [45] A. Vaswani, N. Shazeer, N. Parmar, J. Uszkoreit, L. Jones, A. N. Gomez, Ł. Kaiser, and I. Polosukhin. Attention is all you need. *Advances in neural information processing systems*, 30, 2017. [1](#)
- [46] H. Wang, Z. Wang, M. Du, F. Yang, Z. Zhang, S. Ding, P. Mardziel, and X. Hu. Score-cam: Score-weighted visual explanations for convolutional neural networks. In *Proceedings of the IEEE/CVF conference on computer vision and pattern recognition workshops*, pages 24–25, 2020. [1](#)
- [47] Q. You, H. Jin, Z. Wang, C. Fang, and J. Luo. Image captioning with semantic attention. In *Proceedings of the IEEE conference on computer vision and pattern recognition*, pages 4651–4659, 2016. [4](#)
- [48] O. Zaidan, J. Eisner, and C. Piatko. Using “annotator rationales” to improve machine learning for text categorization. In *Human language technologies 2007: The conference of the North American chapter of the association for computational linguistics; proceedings of the main conference*, pages 260–267, 2007. [2](#)
- [49] B. Zhou, A. Khosla, A. Lapedriza, A. Oliva, and A. Torralba. Learning deep features for discriminative localization, 2015. [1](#), [3](#), [7](#)
- [50] B. Zhou, A. Lapedriza, A. Khosla, A. Oliva, and A. Torralba. Places: A 10 million image database for scene recognition. *IEEE Transactions on Pattern Analysis and Machine Intelligence*, 2017. [4](#)
- [51] B. Zhou, Y. Sun, D. Bau, and A. Torralba. Interpretable basis decomposition for visual explanation. In *Proceedings of the European Conference on Computer Vision (ECCV)*, pages 119–134, 2018. [1](#)